Inorganic Chemistry

pubs.acs.org/IC

Article

Tailoring the Surface Properties of Bi_2O_2NCN by *in Situ* Activation for Augmented Photoelectrochemical Water Oxidation on WO_3 and $CuWO_4$ Heterojunction Photoanodes

Zheng Chen, Alex J. Corkett, Caspar de Bruin-Dickason, Jianhong Chen, Anna Rokicińska, Piotr Kuśtrowski, Richard Dronskowski, and Adam Slabon*

Cite This: *Inorg. Chem.* 2020, 59, 13589−13597

Read Online

ACCESS | Metrics & More | Article Recommendations | Supporting Information

ABSTRACT: Bismuth(III) oxide-carbodiimide (Bi_2O_2NCN) has been recently discovered as a novel mixed-anion semiconductor, which is structurally related to bismuth oxides and oxysulfides. Given the structural versatility of these layered structures, we investigated the unexplored photochemical properties of the target compound for photoelectrochemical (PEC) water oxidation. Although Bi_2O_2NCN does not generate a noticeable photocurrent as a single photoabsorber, the fabrication of heterojunctions with the WO_3 thin film electrode shows an upsurge of current density from 0.9 to 1.1 mA cm^{-2} at 1.23 V vs reversible hydrogen electrode (RHE) under 1 sun (AM 1.5G) illumination in phosphate electrolyte (pH 7.0). Mechanistic analysis and structural analysis using powder X-ray diffraction (XRD), scanning electron microscopy (SEM), X-ray photoelectron spectroscopy (XPS), and scanning transmission electron microscopy energy-dispersive X-ray spectroscopy (STEM EDX) indicate that Bi_2O_2NCN transforms during operating conditions *in situ* to a core−shell structure $Bi_2O_2NCN/BiPO_4$. When compared to $WO_3/BiPO_4$, the *in situ* electrolyte-activated WO_3/Bi_2O_2NCN photoanode shows a higher photocurrent density due to superior charge separation across the oxide/oxide-carbodiimide interface layer. Changing the electrolyte from phosphate to sulfate results in a lower photocurrent and shows that the electrolyte determines the surface chemistry and mediates the PEC activity of the metal oxide-carbodiimide. A similar trend could be observed for $CuWO_4$ thin film photoanodes. These results show the potential of metal oxide-carbodiimides as relatively novel representatives of mixed-anion compounds and shed light on the importance of the control over the surface chemistry to enable the *in situ* activation.

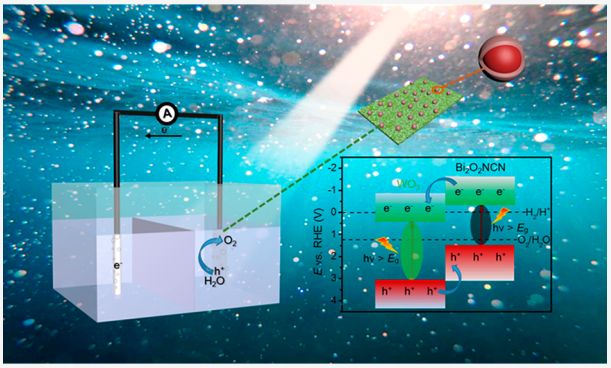

INTRODUCTION

The development of clean, renewable, and long-term sustainable energy sources to help prevent impending climate change while sustaining the global population and economic growth is a colossal challenge.[1,2] To this end, harnessing solar energy through energy conversion technologies represents a promising piece of the puzzle.[2−7] One such pathway uses PEC cells to obtain hydrogen from water upon solar illumination.[7−10] Photochemical water-splitting includes the hydrogen evolution reaction (HER) and the oxygen evolution reaction (OER), which have to be accomplished simultaneously.[11] Kinetics and stability are considered to be critical issues in the water-splitting process, which limits the PEC water-splitting efficiency.[12] Currently, significant efforts are focused on developing efficient photoanodes to accelerate the sluggish four-electron transfer oxidation reaction and reduce energy consumption.[13−16]

A plethora of various semiconductors have been extensively investigated, including binary and ternary oxides.[17−22] Because the semiconductor surface suffers from low catalytic activity, it is crucial to optimize the charge transport ability and recombination rate of the photogenerated carriers.[23] Modifying the photoanode of a light-absorption semiconductor with photoelectrocatalysts or electrocatalysts is a promising strategy to tackle the kinetics demand.[24−27]

Different light absorbers and electrocatalysts has been used to construct advantageous heterojunction photoanodes.[7,28−31] Bismuth(III) based semiconductors, such as Bi_2O_3, $BiPO_4$, $BiVO_4$, and the mixed-anion compounds Bi_2O_2S and BiOCl, have received much attention as photoanodes for PEC water-splitting.[32−42] The merits of such bismuth oxides include nontoxicity, low cost, chemical stability, and good photo-

Received: July 1, 2020
Published: September 4, 2020

https://dx.doi.org/10.1021/acs.inorgchem.0c01947
Inorg. Chem. 2020, 59, 13589−13597

chemical transport properties which are proposed to originate from the dispersed nature of the Bi states in the vicinity of the valence band edge (VBE) and conduction band edge (CBE), thereby providing efficient electron−hole separation.[38]

Meanwhile, metal carbodiimides have recently drawn considerable interest as novel materials in photochemical energy conversion systems.[43−48] Indeed, composite heterojunction photoanodes modified with metal carbodiimides have been shown to display a high charge separation efficiency.[46] Up to now, there has only been one example of the application of mixed-anion compounds based on a metal oxide-carbodiimide, i.e., Sn_2ONCN, for water-splitting.[48] We recently discovered the novel compound Bi_2O_2NCN, which is a semiconductor with an electronic band gap of 1.8 eV and displays a layered structure.[49] Driven by curiosity regarding if this compound may be also suited for water oxidation, we have discovered in our present study that the title compound undergoes an electrolyte-mediated *in situ* activation when coupled to WO_3 and $CuWO_4$ photoanodes.

EXPERIMENTAL SECTION

Synthesis of Bi_2O_2NCN. Bi_2O_2NCN was prepared in an argon-filled glovebox by a solid-state metathesis reaction.[49] BiOCl and Na_2NCN were mixed in a 2:1 molar ratio and ground in an agate mortar under argon. The reaction mixture of 500 mg was sealed in an open dry glass capillary (8 mm). The obtained sample was then placed in a glass ampule and was heated in a tube furnace under flowing argon gas to 350 °C for 2 h, with heating and cooling rates of 2 °C min^{-1}. The resultant powder was subsequently opened in air. After being washed with deionized water and dried in an oven at 80 °C for 4 h, the product Bi_2O_2NCN was obtained.

Synthesis of $BiPO_4$. A 0.485 g portion of $Bi(NO_3)_3{\cdot}5H_2O$ was dissolved in 90 mL of aqueous solution containing 10% glycerol by ultrasound. When completely dissolved, 0.136 g of KH_2PO_4 was added into the above mixture under vigorous stirring which was maintained under stirring for 2 h. The resultant white suspension was centrifuged and washed alternately with deionized water and ethanol three times before being oven-dried at 120 °C for 8 h to obtain a powder sample of hexagonal $BiPO_4$.[50]

Synthesis of WO_3 Thin Films. WO_3 thin films were produced on fluorine doped tin oxide (FTO) glass (4 cm × 1.8 cm, 2.2 mm thick, Sigma-Aldrich) by a hydrothermal synthesis method. FTO substrates were ultrasonically cleaned in diluted nitric acid, acetone, and ethanol for 15 min each in sequence and then dried in an ambient atmosphere. A 0.165 g portion of sodium tungstate dihydrate ($Na_2WO_4{\cdot}2H_2O$, 99.9%, Acros Organics) and a 0.126 g portion of $H_2C_2O_4{\cdot}2H_2O$ were dissolved in 5 and 10 mL of deionized water by stirring, respectively. The two solutions were then mixed with stirring, and 10 mL of 1 M HCl was added and stirred for 10 min. A 6 mL portion of the mixed solution was transferred to a 20 mL Teflon-lined stainless steel autoclave, where a FTO substrate was placed inside with the conducting side facing down and leaning against the inner wall. The autoclave was tightly sealed and heated at 180 °C for 2 h, and then it was cooled to room temperature. After that, the FTO glass was cautiously washed with water and dried in the air. The monoclinic WO_3 thin film grown on an FTO substrate could be achieved after annealing at 550 °C for 1 h and then cooling to room temperature under an ambient atmosphere.

Synthesis of $CuWO_4$ Thin Films. $CuWO_4$ electrodes were prepared as in our previous work.[48] A 1.26 g portion of sodium tungstate dihydrate ($Na_2WO_4{\cdot}2H_2O$, 99.9%, Acros Organics) was dissolved in 15 mL of deionized water, and 1 mL hydrogen peroxide (30%) was added to the tungstate solution. The latter was stirred for 20 min at room temperature. A 25 mL portion of deionized water and 25 mL of isopropanol (>99.7%,) were added to the solution. A 0.73 g portion of copper(II) nitrate trihydrate ($Cu(NO_3)_2{\cdot}3H_2O$, >99%, Sigma) in 10 mL of deionized water was added to the tungsten precursor solution. The pH value was adjusted to 1.2 by nitric acid, and the solution was used for electrochemical deposition on FTO glass. The deposition was performed in a three-electrode setup with platinum wire and 1 M Ag/AgCl as a counter electrode and a reference electrode, respectively. The potential was swept in the range from −0.9 to +0.2 V vs 1 M Ag/AgCl for 12 cycles at a scan rate of 50 mV s^{-1}. After that, the working electrode was washed with deionized water, dried at room temperature, and heated at 450 °C for 2 h under ambient atmosphere. The excess copper oxide was etched by immersing the electrode into 0.5 M HCl for acidic treatment. The $CuWO_4$ thin film grown on FTO substrate could be achieved after annealing one more time at 450 °C for 30 min under ambient atmosphere.

Preparation of Bi_2O_2NCN, $BiPO_4$, WO_3/Bi_2O_2NCN, $WO_3/BiPO_4$, $CuWO_4/Bi_2O_2NCN$, and $CuWO_4/BiPO_4$ Photoanodes. The photoanodes were prepared by a drop-coating method. Bi_2O_2NCN (or $BiPO_4$) powders were dispersed in ethanol (100 μg mL^{-1}) by ultrasound. Cleaned FTO, WO_3, and $CuWO_4$ thin film electrodes were placed on a heating plate at 50 °C. The Bi_2O_2NCN (or $BiPO_4$) dispersion was drop-cast on the surfaces of the corresponding electrodes. The Bi_2O_2NCN, $BiPO_4$, WO_3/Bi_2O_2NCN, $WO_3/BiPO_4$, and $CuWO_4/Bi_2O_2NCN$ and $CuWO_4/BiPO_4$ photoanodes were obtained after drying under an ambient atmosphere.

Deposition of Cobalt Phosphate (CoP_i) Layer. Photoassisted electrodeposition of CoP_i on the WO_3/Bi_2O_2NCN and $CuWO_4/Bi_2O_2NCN$ electrodes was carried out under illumination at a constant potential of 0.25 V vs 1 M Ag/AgCl for 15 s in a 0.5 mM $Co(NO_3)_2$ solution with 0.1 M phosphate buffer electrolyte.

Structural Characterization. Powder XRD patterns were recorded in transmission mode on a STOE STADI-P diffractometer (Cu Kα_1 radiation) operating with a DECTRIS Mythen 1K detector at a scan rate of 2° min^{-1} in the 2θ range from 10° to 90°.

SEM images were recorded on a Leo Supra 35VP SMT (Zeiss) thermal field emission scanning electron microscope operating at an accelerating voltage of 10.0 kV.

TEM images were recorded on a Themis Z TEM (Thermo Fisher), and a SuperX energy-dispersive X-ray (EDX) detector operating at 300 kV in the scanning TEM mode was used for elemental mapping.

XPS spectra were recorded by a hemispherical VG SCIENTA R3000 analyzer using a monochromatized aluminum source Al Kα (E = 1486.6 eV) at constant pass energy of 100 eV. The binding energies were referenced to the Au 4f core level (E_b = 84.0 eV). The composition and chemical surrounding of the sample surface were determined on the basis of the areas and binding energies of Na 1s, K 2p, P 2p, O 1s, N 1s, C 1s, and Bi 4f photoelectron peaks. The fitting of the high-resolution spectra was obtained through the Casa XPS software.

Ultraviolet−visible (UV−vis) spectroscopy was performed on a Shimadzu UV-2600 spectrophotometer. Measurements were recorded in absorbance mode. The Tauc plots were calculated by the Kubelka−Munk function $F(R) = (1 - R)^2/2R$ for determination of the electronic band gap.

PEC Measurements. The PEC experiments were measured with a potentiostat (Gamry instruments) using an electrochemical cell operating in a three-electrode setup system. In this system, the photoanode, platinum wire, and a 1 M Ag/AgCl electrode function as a working electrode, counter electrode, and reference electrode, respectively. All current values of the electrodes were recorded vs 1 M Ag/AgCl reference electrode and converted to vs RHE according to E_{RHE} (V) = $E_{1MAg/AgCl}$ (V) + 0.235 (V) + [0.059 × pH] (V) at 25 °C. A solar light simulator (class-AAA 94023A, Newport) with an ozone-free 450 W xenon short-arc lamp was used to illuminate the photoanode with AM 1.5G simulated visible light, which was calibrated with a Si reference cell (LOT-Quantum Design, Germany). Milli-Q water (18.3 Ω cm) was used to prepare the 0.1 M potassium phosphate (KP_i) electrolytes. The linear square voltammetry (LSV) was recorded with a scan rate of 10 mV s^{-1} in the range 0.64−1.44 V vs RHE, and chronoamperometry (CA) was recorded at 1.23 V vs RHE. Mott−Schottky (MS) measurements were performed in an electromagnetically shielded box with an applied frequency of 100 Hz.

https://dx.doi.org/10.1021/acs.inorgchem.0c01947
Inorg. Chem. 2020, 59, 13589−13597

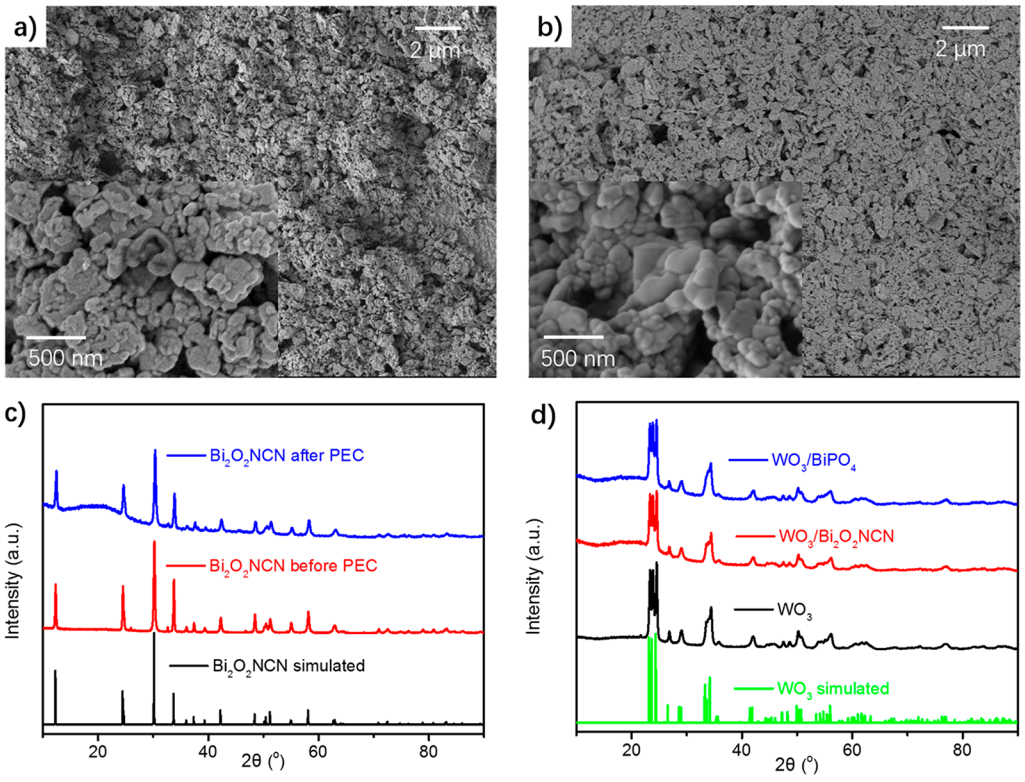

Figure 1. SEM micrograph of Bi_2O_2NCN (a) before and (b) after PEC water oxidation. (c) Simulated XRD patterns of Bi_2O_2NCN and experimental powder XRD patterns of Bi_2O_2NCN. (d) Simulated XRD patterns of WO_3 and experimental powder XRD patterns of WO_3, WO_3/Bi_2O_2NCN, and WO_3/$BiPO_4$.

An electrochemical impedance spectroscopy (EIS) Nyquist plot was recorded at a bias of 1 V vs RHE under AM 1.5G illumination.

RESULTS AND DISCUSSION

Structure and Characterization. Bi_2O_2NCN is a compound with an extended anti-$ThCr_2Si_2$-type structure and crystallizes with the space group *I*4/*mmm*. An important structural feature of Bi_2O_2NCN is the presence of fluorite-type layers of edge-sharing $[Bi_4O]$ tetrahedra, equivalent to those in BiOCl, alternating with NCN^{2-} layers. Moreover, Bi_2O_2NCN is in fact isostructural to Bi_2O_2Ch oxide chalcogenides (Ch = S, Se, and Te; n.b., the S analogue adopts an orthorhombically distorted low-symmetry modification), thereby highlighting the divalent nitride or pseudochalcogenide nature of NCN^{2-}.[49] The higher degree of electronegativity of NCN^{2-} relative to sulfide yields a band gap that is intermediate between that of Bi_2O_2S (1.12 eV) and β-Bi_2O_3 (2.48 eV) (Figure S1).[51,52] For structural characterization, a portion of the Bi_2O_2NCN photoanode was physically removed after PEC OER in KP_i at pH 7.0. SEM images show that the Bi_2O_2NCN exhibits porous globular shapes, the morphology of which shows no visible change before (Figure 1a) and after (Figure 1b) PEC water oxidation. The PXRD patterns of Bi_2O_2NCN show that the compound is structurally stable in the bulk (Figure 1c). Due to the low amount of catalyst loading to WO_3 thin films, the corresponding PXRD patterns of the modified photoanodes contain only the diffraction peaks of WO_3, which remain unchanged after PEC OER (Figure 1d).

The band gaps of Bi_2O_2NCN and WO_3 were determined from the UV−vis absorption spectra (Figure 2a,b). After conversion to Kubelka−Munk-transformed reflectance spectra, the band gaps of Bi_2O_2NCN and WO_3 were determined to be

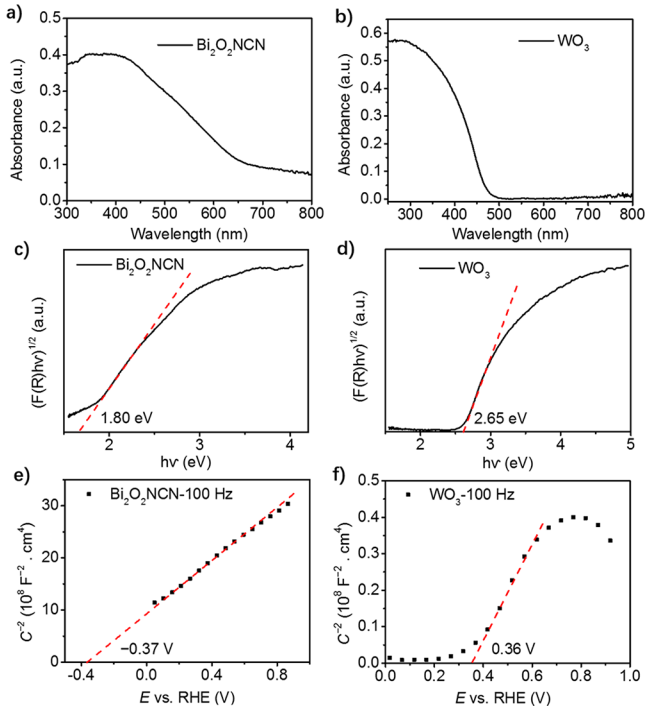

Figure 2. UV−vis absorption spectra (a, b), Kubelka−Munk-transformed reflectance spectra (c, d), and MS plot (e, f) of Bi_2O_2NCN and WO_3.

1.80 eV (Figure 2c) and 2.65 eV (Figure 2d), respectively. For Bi_2O_2NCN, the MS plot reveals a positive slope indicating n-type semiconductor behavior, and extrapolation of the curve

https://dx.doi.org/10.1021/acs.inorgchem.0c01947
Inorg. Chem. 2020, 59, 13589−13597

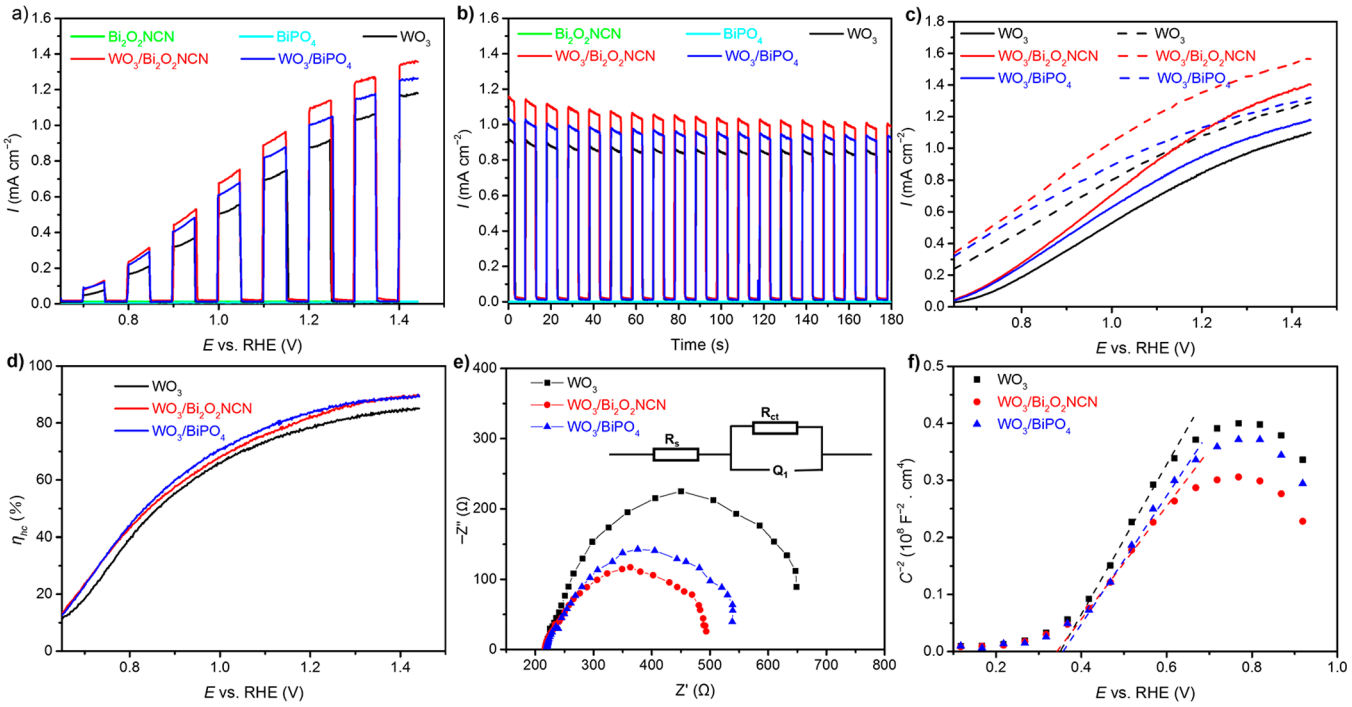

Figure 3. (a) LSV and (b) CA in KP_i electrolyte at 1.23 V vs RHE of Bi_2O_2NCN, $BiPO_4$, WO_3, WO_3/Bi_2O_2NCN, and $WO_3/BiPO_4$ photoanodes; (c) the photocurrent densities during water (solid line) and sulfite oxidation (dashed line) for WO_3 (black), WO_3/Bi_2O_2NCN (red), and $WO_3/BiPO_4$ (blue) photoanodes; (d) η_{hc} of WO_3, WO_3/Bi_2O_2NCN, and $WO_3/BiPO_4$ photoanodes; (e) EIS Nyquist plots of WO_3, WO_3/Bi_2O_2NCN, and $WO_3/BiPO_4$ photoanodes at a bias of 1 V vs RHE, with the inset showing the equivalent circuit model; and (f) MS analysis of WO_3, WO_3/Bi_2O_2NCN, and $WO_3/BiPO_4$ photoanodes with an applied frequency of 100 Hz.

shows that the flat band potential is equal to −0.37 V vs RHE (Figure 2e). From the band gap and flat band potential, which is close to the value of the CBE for n-type semiconductor, the values of VBE and CBE are 1.43 V and −0.37 V vs RHE, respectively. Similarly, the VBE and CBE of WO_3 are 3.01 and 0.36 V vs RHE (Figure 2f), and the VBE and CBE of $BiPO_4$ are 3.53 V and −0.61 V vs RHE, respectively (Figure S2).

Photoelectrochemistry. Bi_2O_2NCN was employed to produce type-II heterojunctions with a WO_3 thin film to obtain a composite photoanode. Simultaneously, we made Bi_2O_2NCN, WO_3, $BiPO_4$, and $WO_3/BiPO_4$ photoanodes for comparison. $BiPO_4$ was chosen to evaluate the possible interaction between the phosphate anions of the electrolyte with the Bi_2O_2NCN particles (*vide infra*). LSV curves were collected in 0.1 M KP_i electrolyte at pH 7.0 under chopped AM 1.5G illumination (backlight). For the WO_3 photoanode, the LSV result exhibits only a photocurrent density of approximately 0.90 mA cm^{-2} when measured at 1.23 V vs RHE under AM 1.5G illumination, indicating significant electron−hole recombination (Figure 3a).

Upon functional modification with Bi_2O_2NCN and $BiPO_4$, an upsurge of current density to 1.10 and 1.00 mA cm^{-2} manifested under the same conditions, respectively (Figure 3a). This upsurge was achieved upon addition of 12 μg of Bi_2O_2NCN and 8 μg of $BiPO_4$, respectively (Figure S3). In contrast, the bare Bi_2O_2NCN and $BiPO_4$ photoanodes with the same amount of material as for the composite photoanode developed only a negligible photocurrent density under the same operation conditions. Significantly, the produced photocurrent density of the composite photoanodes is higher than the sum of its individual components, indicating that a synergistic effect occurs between the WO_3 and Bi_2O_2NCN or $BiPO_4$ catalysts. This trend is more visible in CA at 1.23 V vs RHE under chopped backlight AM 1.5G illumination (Figure 3b). The improved PEC activity was consistent with the increase of IPCE after functionalization with Bi_2O_2NCN (Figure S4). The prolonged CA of the composite electrode is shown in Figure S5.

To understand the origin of the increased photocurrent density upon modification, the hole collection efficiency (η_{hc} measured) was studied by introducing Na_2SO_3 as a hole scavenger. The oxidation reaction of sulfite to sulfate is faster than the oxidation of water. Measurements were performed in 0.1 M KP_i (pH 7.0) with or without 0.05 M Na_2SO_3 under backlight AM 1.5G illumination (Figure 3c). In this way, the number of holes reaching the semiconductor−electrolyte interface in the reaction can be estimated. The η_{hc} can be calculated by the ratio of photocurrent density for oxidation of sulfite (J_{Na2SO3}) and water (J_{H2O}): $\eta_{hc} = J_{H2O}/J_{Na2SO3}$. In comparison with the WO_3 photoanode, the η_{hc} of the composite photoanode is increased (Figure 3d), indicating that the reactivity of the surface is augmented after modification with Bi_2O_2NCN or $BiPO_4$. It should be noted that functionalization with $BiPO_4$ gave slightly higher η_{hc} values between 0.8 and 1.23 V in comparison to the Bi_2O_2NCN-derived phosphate catalyst. Nevertheless, the advantage of the latter is the semiconducting core for improved charge separation.

To investigate the kinetics of charge transfer in the composite electrode system, we carried out EIS measurements. Figure 3e shows the EIS Nyquist plots which were measured in KP_i electrolyte (pH 7) at a bias of 1 V RHE under AM 1.5G illumination. The Nyquist plot could be interpreted by the equivalent circuit as displayed in the inset. In the equivalent circuit, R_s simulates the series resistance, Q_1 simulates the constant phase element (CPE) for the electrolyte/electrode

https://dx.doi.org/10.1021/acs.inorgchem.0c01947
Inorg. Chem. 2020, 59, 13589−13597

interface, and R_{ct} simulates the charge transfer resistance across the electrode/electrolyte interface. Compared with the semicircle of the WO_3 photoanode, the smaller semicircle of the heterojunction photoanode demonstrates that the charge-carrier conductivity is improved after modification with Bi_2O_2NCN or $BiPO_4$.

MS analysis was conducted in 0.1 M KP_i electrolyte with an applied frequency of 100 Hz. The positive slopes of the plots are in agreement with the expected n-type behavior, while the reduced slope after modification of WO_3 hints toward improved charge-carrier transport (Figure 3f). Furthermore, the charge-carrier density of WO_3@Bi_2O_2NCN was higher than that of WO_3@bare $BiPO_4$. The determined flat band potentials are within the range of WO_3, i.e., the relatively bulk thin film before modification.

Structural Analysis after PEC Water Oxidation. To further identify the origin for improved PEC activity after modification, we analyzed the surface properties of a Bi_2O_2NCN photoanode by XPS and TEM after an extended PEC experiment in a 0.1 M KP_i electrolyte (pH 7.0) under AM 1.5G illumination. The survey XP spectrum of the photoanode surface confirms the presence of all expected elements, including C, N, O, Na, K, P, and Bi. The high-resolution XPS Bi 4f spectrum (Figure 4) shows two doublets with the

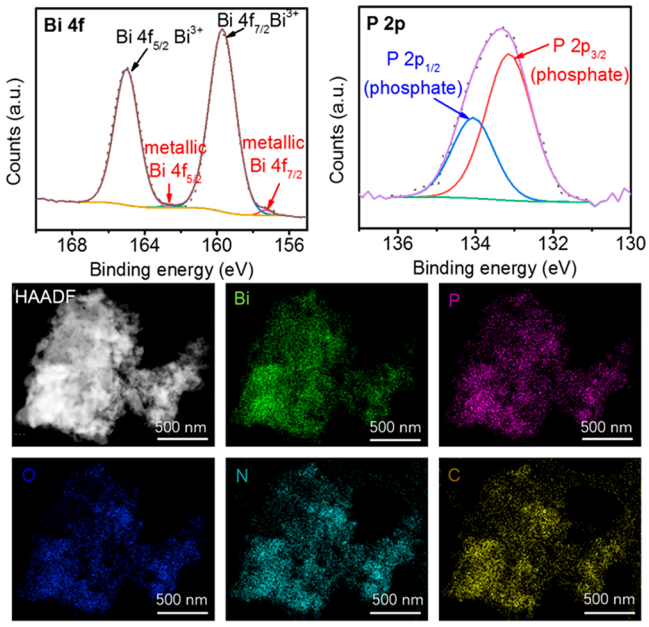

Figure 4. XPS spectrum and HAADF micrograph with corresponding STEM EDX elemental mapping of the Bi_2O_2NCN photoanode after PEC water oxidation.

splitting energies of 5.3 eV.[53−55] The dominant doublet, corresponding to the Bi^{3+} species, is observed at 159.7 eV (Bi $4f_{7/2}$) and 165.0 eV (Bi $4f_{5/2}$). Furthermore, traces of metallic Bi appear on the surface, which are manifested by the photoemission at 157.3 eV (Bi $4f_{7/2}$) and 162.6 eV (Bi $4f_{5/2}$). It can be assumed that a significant amount of bismuth forms the phosphate phase, i.e., a core−shell structure Bi_2O_2NCN@$BiPO_x$. The formation of this shell is confirmed by the XPS P 2p spectrum (Figure 4), in which two peaks at 133.1 eV (P $2p_{3/2}$) and 134.0 eV (P $2p_{1/2}$) typical of phosphate species are identified. Phosphorus was also structurally determined by TEM EDX analysis (Figure 4).

Complementary structural analysis by means of high-angle annular dark field (HAADF) images shows the elemental mapping obtained with EDX. The presence of bismuth, oxygen, nitrogen, carbon, and phosphorus was also confirmed, which indicates that the carbodiimide is not further oxidized upon formation of the protective phosphate shell. The situation is therefore comparable to the stabilization of metastable metal oxynitride photoanodes. Attempts to characterize the Bi_2O_2NCN electrode after PEC water oxidation by means of HRTEM were not successful due to beam damage. Figure S6a shows the TEM image of the Bi_2O_2NCN particles, which decomposed rapidly into Bi_2O_3 nanosheets (Figure S6b−d). The beam damage is highly likely due to the carbodiimide anion of the Bi_2O_2NCN.

On the basis of a combination of XPS, TEM, SEM, and XRD analyses, the improved WO_3 photoanode performance after modification with Bi_2O_2NCN is attributed to the formation of an oxide/oxide-carbodiimide heterojunction. A phosphate-type shell on the Bi_2O_2NCN surface was formed after the PEC experiment in a phosphate electrolyte. The catalytic activation of the heterojunction was formed between the $BiPO_x$ shell with Bi_2O_2NCN core and WO_3. The observed PEC behavior of Bi_2O_2NCN is different from CoNCN, which retains the same chemical composition on the surface and the bulk but is similar to MnNCN.[44,47] The latter is known to form an amorphous manganese phosphate shell.

A control experiment was conducted to investigate the effect of the electrolyte-mediation on the PEC behavior. LSV and CA results show that the WO_3 photoanode has almost identical photocurrent density in 1 M Na_2SO_4 electrolyte and 0.1 M KP_i electrolyte at 1.23 V vs RHE under illumination (Figure 5). It is worth mentioning that the WO_3 electrode starts to produce higher photocurrents in Na_2SO_4 electrolyte than in KP_i electrolyte above approximately 1.20 V vs RHE. Since most CA data are compared in the literature at 1.23 V vs RHE, we have chosen the thermodynamic potential for the CA. After modification with Bi_2O_2NCN, a higher photocurrent density is generated in KP_i electrolyte than in Na_2SO_4 at 1.23 V vs RHE (Figure 5b). This result indicates bismuth phosphate to have the dominant role to augment the charge-carrier transport.

The interface formation of semiconductors with different VBE and CBE positions can result in improved charge-carrier separation.[35] The energy band diagram for the given semiconductors sheds light on the origin (Figure 6). Compared with the CBE position of WO_3, the higher CBE position of Bi_2O_2NCN facilitates the injection of photogenerated electrons into WO_3 with a concomitant diffusion of the photogenerated holes from WO_3 to Bi_2O_2NCN. WO_3/$BiPO_4$ and WO_3/Bi_2O_3 heterojunction catalysts have been previously evaluated with respect to their PEC degradation of rhodamine B.[56−58] These results demonstrate an increased region of the absorption spectrum under visible light illumination and an efficient transfer and separation of charge carriers by synergistic effect between its components. Moreover, a surface oxygen vacancy may also be induced for WO_3/Bi_2O_2NCN@$BiPO_x$, which is a complex structure system.[59,60] As a result, a synergistic effect of the novel WO_3/Bi_2O_2NCN@$BiPO_x$ heterojunctions led to a boosted photocatalytic performance of the reaction system.

We investigated whether Bi_2O_2NCN can be coupled with other semiconductor materials besides the binary WO_3 to form a heterojunction photoanode with improved performance.

https://dx.doi.org/10.1021/acs.inorgchem.0c01947
Inorg. Chem. 2020, 59, 13589−13597

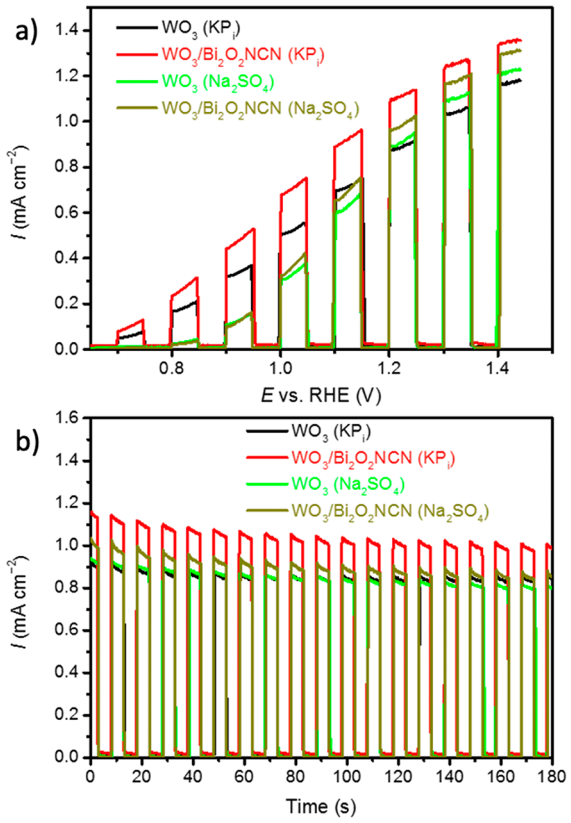

Figure 5. LSV and CA at 1.23 V vs RHE of WO_3 and WO_3/Bi_2O_2NCN photoanodes. Measurements were performed in 0.1 M KP_i electrolyte (pH 7.0) and 1 M Na_2SO_4 (pH 7) under sequentially interrupted AM 1.5G illumination, respectively.

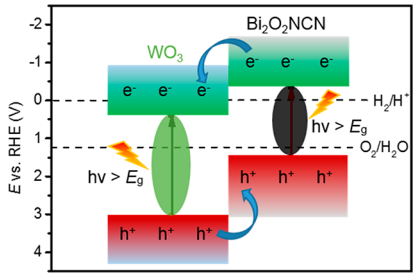

Figure 6. Energy band diagram of the heterojunction WO_3/Bi_2O_2NCN.

We chose the ternary oxide $CuWO_4$ which exhibits a narrower band gap than the current best-performing oxidic semiconductor $BiVO_4$ used for photoanodes.[48] Similar to the measurements on the WO_3 photoanodes, the fabricated thin films of $CuWO_4$ were evaluated for PEC water oxidation with respect to the following parameters: (i) sulfate vs phosphate electrolyte and (ii) Bi_2O_2NCN vs $BiPO_4$. The summarized results of the LSV and CA presented in Figure 7 show that the *in-situ*-activated Bi_2O_2NCN outperforms $BiPO_4$. The photocurrent density of the composite photoanode is increased by 85% at 1.23 V vs RHE upon modification with Bi_2O_2NCN in comparison to the pristine $CuWO_4$ photoanode. These observations are consistent with the results obtained for the WO_3 photoanodes and demonstrate that the Bi_2O_2NCN@$BiPO_4$ core−shell structure, which is only formed in the phosphate electrolyte, can be successfully applied to other oxide semiconductors if the band gaps are matched. Moreover,

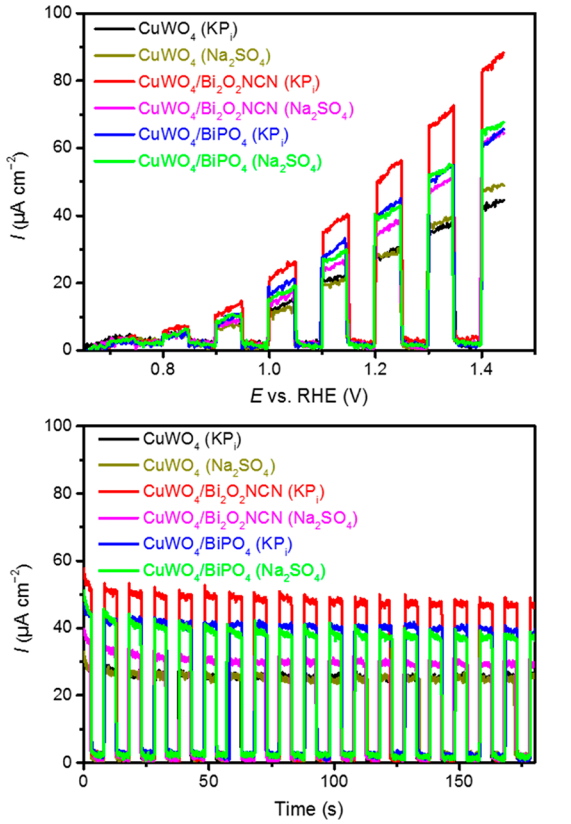

Figure 7. LSV and CA at 1.23 V vs RHE of $CuWO_4$, $CuWO_4$/Bi_2O_2NCN, and $CuWO_4$/$BiPO_4$ photoanodes. Measurements were performed in 0.1 M KP_i electrolyte (pH 7.0) and 1 M Na_2SO_4 (pH 7) under sequentially interrupted AM 1.5G illumination, respectively. Note that the current densities are almost identical for pristine $CuWO_4$ photoanodes in both electrolytes.

the PEC OER could be increased after modification with a layer of CoP_i as cocatalyst on the surface of WO_3/Bi_2O_2NCN and $CuWO_4$/Bi_2O_2NCN photoanodes (Figure 8).

CONCLUSION

The photochemical behavior of Bi_2O_2NCN and its application as a functional modification material to WO_3 and $CuWO_4$ electrodes for PEC OER have been investigated. The modified photoanode shows an augmented photocurrent effect during PEC water oxidation as a consequence of electrolyte-mediated *in situ* activation to a Bi_2O_2NCN@$BiPO_4$ core−shell structure, which has been confirmed by complementary XPS, XRD, and STEM EDX analysis. The Bi_2O_2NCN@$BiPO_4$ core−shell structure outperforms a bare $BiPO_4$ catalyst while the semiconducting oxide-carbodiimide core facilitates charge-carrier separation across the formed type-II heterojunction. Changing the electrolyte from phosphate to sulfate results in a lower photocurrent and shows that the electrolyte determines the surface chemistry and mediates the PEC activity of the metal oxide-carbodiimide. The results illustrate the potential of metal oxide-carbodiimides as relatively novel representatives of mixed-anion compounds. The study demonstrates that the incorporation of the less ionic carbodiimide anion into an oxidic structure increases the theoretical light absorption, but that at the same time the labile NCN^{2-} anion opens opportunities to tailor the surface chemistry to alter charge transfer kinetics.

https://dx.doi.org/10.1021/acs.inorgchem.0c01947
Inorg. Chem. 2020, 59, 13589−13597

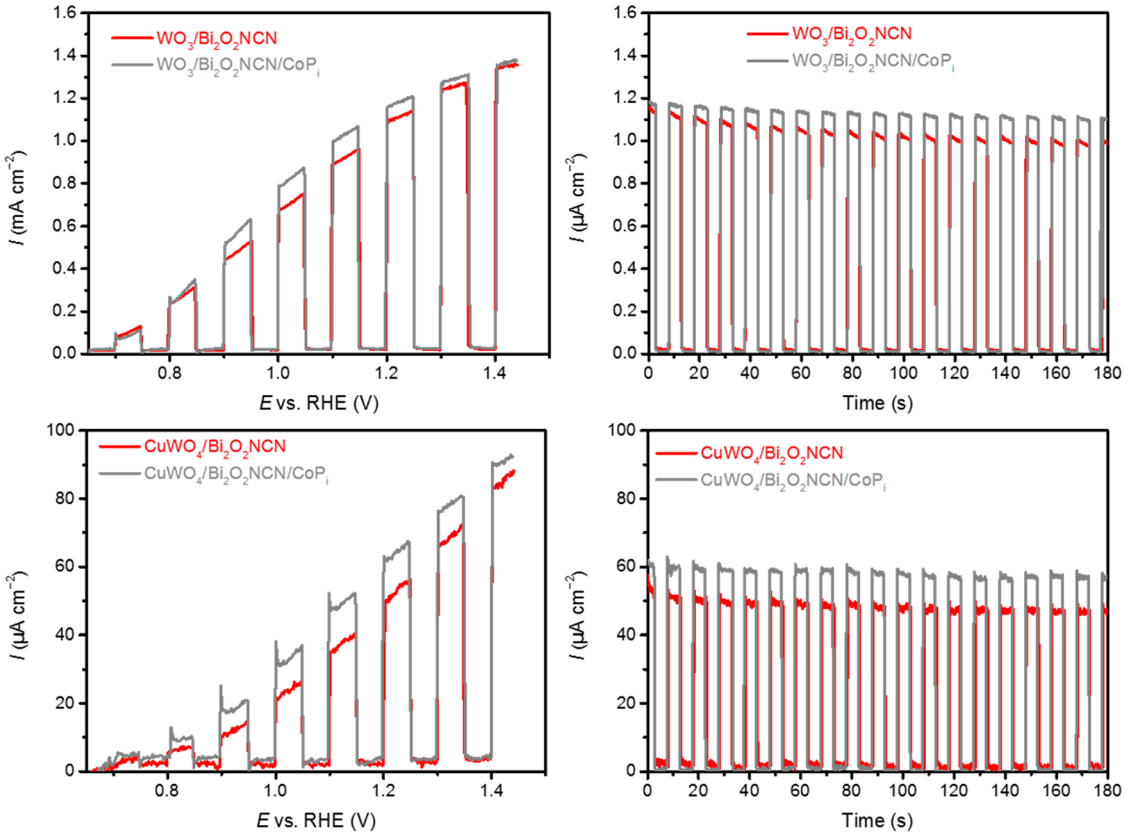

Figure 8. LSV and CA at 1.23 V vs RHE of $WO_3/Bi_2O_2NCN/CoP_i$ and $CuWO_4/Bi_2O_2NCN/CoP_i$ photoanodes. Measurements were performed in 0.1 M KP_i electrolyte (pH 7.0) under sequentially interrupted illumination on new electrodes.

■ ASSOCIATED CONTENT

Supporting Information

The Supporting Information is available free of charge at https://pubs.acs.org/doi/10.1021/acs.inorgchem.0c01947.

Electronic structures of α-Bi_2O_3, β- Bi_2O_3, Bi_2O_2NCN, $BiPO_4$, and WO_3; structural characterization of $BiPO_4$; complementary LSV and CA curves for electrodes; additional XRD patterns of synthesized materials; and TEM images illustrating beam damage of Bi_2O_2NCN sample (PDF)

■ AUTHOR INFORMATION

Corresponding Author

Adam Slabon − *Department of Materials and Environmental Chemistry, Stockholm University, 10691 Stockholm, Sweden;* orcid.org/0000-0002-4452-1831; Email: adam.slabon@mmk.su.se

Authors

Zheng Chen − *Solid-State and Quantum Chemistry, Institute of Inorganic Chemistry, RWTH Aachen University, 52056 Aachen, Germany*

Alex J. Corkett − *Solid-State and Quantum Chemistry, Institute of Inorganic Chemistry, RWTH Aachen University, 52056 Aachen, Germany;* orcid.org/0000-0002-7725-2498

Caspar de Bruin-Dickason − *Department of Materials and Environmental Chemistry, Stockholm University, 10691 Stockholm, Sweden*

Jianhong Chen − *Department of Materials and Environmental Chemistry, Stockholm University, 10691 Stockholm, Sweden*

Anna Rokicińska − *Faculty of Chemistry, Jagiellonian University, 30-387 Krakow, Poland*

Piotr Kuśtrowski − *Faculty of Chemistry, Jagiellonian University, 30-387 Krakow, Poland*

Richard Dronskowski − *Solid-State and Quantum Chemistry, Institute of Inorganic Chemistry, RWTH Aachen University, 52056 Aachen, Germany; Hoffmann Institute of Advanced Materials, Shenzhen Polytechnic, Shenzhen 518055, China;* orcid.org/0000-0002-1925-9624

Complete contact information is available at: https://pubs.acs.org/10.1021/acs.inorgchem.0c01947

Author Contributions

All authors have given approval to the final version of the manuscript.

Notes

The authors declare no competing financial interest.

■ ACKNOWLEDGMENTS

Z.C. thanks the China Scholarship Council for being supported with a PhD scholarship. A.S. acknowledges funding from Vinnova, Sweden's innovation agency (project: C1Bio, reference number 2019-03174). The XPS measurements were carried out with the equipment purchased with the financial support of the European Regional Development Fund in the framework of the Polish Innovation Operational Program (contract POIG.02.01.00-12-023/08). The authors would like to thank Marek Drozdek for performing the XPS experiments.

REFERENCES

(1) Glenk, G.; Reichelstein, S. Economics of Converting Renewable Power to Hydrogen. *Nat. Energy* **2019**, *4*, 216−222.
(2) Wang, Z.; Li, C.; Domen, K. Recent Developments in Heterogeneous Photocatalysts for Solar-Driven Overall Water Splitting. *Chem. Soc. Rev.* **2019**, *48*, 2109−2125.
(3) Grätzel, M. Photoelectrochemical Cells. *Nature* **2001**, *414*, 338−344.
(4) Wang, Q.; Nakabayashi, M.; Hisatomi, T.; Sun, S.; Akiyama, S.; Wang, Z.; Pan, Z.; Xiao, X.; Watanabe, T.; Yamada, T.; Shibata, N.; Takata, T.; Domen, K. Oxysulfide Photocatalyst for Visible-Light-Driven Overall Water Splitting. *Nat. Mater.* **2019**, *18*, 827−832.
(5) Gong, J.; Li, C.; Wasielewski, M. R. Advances in Solar Energy Conversion. *Chem. Soc. Rev.* **2019**, *48*, 1862−1864.
(6) Lewis, N. S. Developing a Scalable Artificial Photosynthesis Technology Through Nanomaterials by Design. *Nat. Nanotechnol.* **2016**, *11*, 1010−1019.
(7) Ye, K.-H.; Li, H.; Huang, D.; Xiao, S.; Qiu, W.; Li, M.; Hu, Y.; Mai, W.; Ji, H.; Yang, S. Enhancing Photoelectrochemical Water Splitting by Combining Work Function Tuning and Heterojunction Engineering. *Nat. Commun.* **2019**, *10*, 3687.
(8) Fujishima, A.; Honda, K. Electrochemical Photolysis of Water at a Semiconductor Electrode. *Nature* **1972**, *238*, 37−38.
(9) He, Y.; Hamann, T.; Wang, D. Thin Film Photoelectrodes for Solar Water Splitting. *Chem. Soc. Rev.* **2019**, *48*, 2182−2215.
(10) Yang, W.; Kim, J. H.; Hutter, O. S.; Phillips, L. J.; Tan, J.; Park, J.; Lee, H.; Major, J. D.; Lee, J. S.; Moon, J. Benchmark Performance of Low-Cost Sb_2Se_3 Photocathodes for Unassisted Solar Overall Water Splitting. *Nat. Commun.* **2020**, *11*, 861.
(11) Hisatomi, T.; Domen, K. Reaction Systems for Solar Hydrogen Production *via* Water Splitting with Particulate Semiconductor Photocatalysts. *Nat. Catal.* **2019**, *2*, 387−399.
(12) Kim, J. H.; Hansora, D.; Sharma, P.; Jang, J.-W.; Lee, J. S. Toward Practical Solar Hydrogen Production − an Artificial Photosynthetic Leaf-to-Farm Challenge. *Chem. Soc. Rev.* **2019**, *48*, 1908−1971.
(13) Jeon, T. H.; Monllor-Satoca, D.; Moon, G.; Kim, W.; Kim, H.; Bahnemann, D. W.; Park, H.; Choi, W. Ag (I) Ions Working as a Hole-Transfer Mediator in Photoelectrocatalytic Water Oxidation on WO_3 Film. *Nat. Commun.* **2020**, *11*, 967.
(14) Lee, D. K.; Lee, D.; Lumley, M. A.; Choi, K. S. Progress on Ternary Oxide-Based Photoanodes for Use in Photoelectrochemical Cells for Solar Water Splitting. *Chem. Soc. Rev.* **2019**, *48*, 2126−2157.
(15) Li, W.; Elzatahry, A.; Aldhayan, D.; Zhao, D. Core−Shell Structured Titanium Dioxide Nanomaterials for Solar Energy Utilization. *Chem. Soc. Rev.* **2018**, *47*, 8203−8237.
(16) Pan, Q.; Li, A.; Zhang, Y.; Yang, Y.; Cheng, C. Rational Design of 3D Hierarchical Ternary $SnO_2/TiO_2/BiVO_4$ Arrays Photoanode toward Efficient Photoelectrochemical Performance. *Adv. Sci.* **2020**, *7*, 1902235.
(17) Sivula, K.; van de Krol, R. Semiconducting Materials for Photoelectrochemical Energy Conversion. *Nat. Rev. Mater.* **2016**, *1*, 15010.
(18) Kim, T. W.; Choi, K.-S. Nanoporous $BiVO_4$ Photoanodes with Dual-Layer Oxygen Evolution Catalysts for Solar Water Splitting. *Science* **2014**, *343*, 990−994.
(19) Huang, M.; Lei, W.; Wang, M.; Zhao, S.; Li, C.; Wang, M.; Zhu, H. Large Area High-Performance Bismuth Vanadate Photoanode for Efficient Solar Water Splitting. *J. Mater. Chem. A* **2020**, *8*, 3845−3850.
(20) Ma, Z.; Linnenberg, O.; Rokicinska, A.; Kuśtrowski, P.; Slabon, A. Augmenting the Photocurrent of $CuWO_4$ Photoanodes by Heat Treatment in the Nitrogen Atmosphere. *J. Phys. Chem. C* **2018**, *122*, 19281−19288.
(21) Hodes, G.; Cahen, D.; Manassen, J. Tungsten Trioxide as a Photoanode for a Photoelectrochemical Cell (PEC). *Nature* **1976**, *260*, 312−313.
(22) Ma, M.; Zhang, K.; Li, P.; Jung, M. S.; Jeong, M. J.; Park, J. H. Dual Oxygen and Tungsten Vacancies on a WO_3 Photoanode for Enhanced Water Oxidation. *Angew. Chem.* **2016**, *128*, 11998−12002.
(23) Wang, Y.; Tian, W.; Chen, C.; Xu, W.; Li, L. Tungsten Trioxide Nanostructures for Photoelectrochemical Water Splitting: Material Engineering and Charge Carrier Dynamic Manipulation. *Adv. Funct. Mater.* **2019**, *29*, 1809036.
(24) Lu, C.; Jothi, P. R.; Thersleff, T.; Budnyak, T. M.; Rokicinska, A.; Yubuta, K.; Dronskowski, R.; Kuśtrowski, P.; Fokwa, B. P. T.; Slabon, A. Nanostructured Core-Shell Metal Boride-Oxide as Highly Efficient Electrocatalysts for Photoelectrochemical Water Oxidation. *Nanoscale* **2020**, *12*, 3121−3128.
(25) Zhou, Y.; Zhang, L.; Lin, L.; Wygant, B. R.; Liu, Y.; Zhu, Y.; Zheng, Y.; Mullins, C. B.; Zhao, Y.; Zhang, X.; Yu, G. Highly Efficient Photoelectrochemical Water Splitting from Hierarchical $WO_3/BiVO_4$ Nanoporous Sphere Arrays. *Nano Lett.* **2017**, *17*, 8012−8017.
(26) Wang, S.; Liu, G.; Wang, L. Crystal Facet Engineering of Photoelectrodes for Photoelectrochemical Water Splitting. *Chem. Rev.* **2019**, *119*, 5192−5247.
(27) Ronconi, F.; Syrgiannis, Z.; Bonasera, A.; Prato, M.; Argazzi, R.; Caramori, S.; Cristino, V.; Bignozzi, C. A. Modification of Nanocrystalline WO_3 with a Dicationic Perylene Bisimide: Applications to Molecular Level Solar Water Splitting. *J. Am. Chem. Soc.* **2015**, *137*, 4630−4633.
(28) Hong, S. J.; Lee, S.; Jang, J. S.; Lee, J. S. Heterojunction $BiVO_4/WO_3$ Electrodes for Enhanced Photoactivity of Water Oxidation. *Energy Environ. Sci.* **2011**, *4*, 1781−1787.
(29) Zhao, Y.; Brocks, G.; Genuit, H.; Lavrijsen, R.; Verheijen, M. A.; Bieberle-Hütter, A. Boosting the Performance of WO_3/n-Si Heterostructures for Photoelectrochemical Water Splitting: from the Role of Si to Interface Engineering. *Adv. Energy Mater.* **2019**, *9*, 1900940.
(30) Kudo, A.; Miseki, Y. Heterogeneous Photocatalyst Materials for Water Splitting. *Chem. Soc. Rev.* **2009**, *38*, 253−278.
(31) Shi, X.; Choi, Y.; Zhang, K.; Kwon, J.; Kim, D. Y.; Lee, J. K.; Oh, S. H.; Kim, J. K.; Park, J. H. Efficient Photoelectrochemical Hydrogen Production from Bismuth Vanadate-Decorated Tungsten Trioxide Helix Nanostructures. *Nat. Commun.* **2014**, *5*, 4775.
(32) Shahbazi, M.-A.; Faghfouri, L.; Ferreira, M. P. A.; Figueiredo, P.; Maleki, H.; Sefat, F.; Hirvonen, J.; Santos, H. A. The Versatile Biomedical Applications of Bismuthbased Nanoparticles and Composites: Therapeutic, Diagnostic, Biosensing, and Regenerative Properties. *Chem. Soc. Rev.* **2020**, *49*, 1253−1321.
(33) Gong, Q.; Ding, P.; Xu, M.; Zhu, X.; Wang, M.; Deng, J.; Ma, Q.; Han, N.; Zhu, Y.; Lu, J.; Feng, Z.; Li, Y.; Zhou, W.; Li, Y. Structural Defects on Converted Bismuth Oxide Nanotubes Enable Highly Active Electrocatalysis of Carbon Dioxide Reduction. *Nat. Commun.* **2019**, *10*, 2807.
(34) Azhar, N. S.; Taib, M. F. M.; Hassan, O. H.; Yahya, M. Z. A.; Ali, A. M. M. Structural, Electronic and Optical Properties of Bi_2O_3 Polymorphs by First-Principles Calculations for Photocatalytic Water Splitting Mater. *Mater. Res. Express* **2017**, *4*, 034002.
(35) Li, Y.; Liu, Z.; Li, J.; Ruan, M.; Guo, Z. An Effective Strategy of Constructing Multi-Junction Structure by Integrating Heterojunction and Homojunction to Promote Charge Separation and Transfer Efficiency of WO_3. *J. Mater. Chem. A* **2020**, *8*, 6256−6267.
(36) Qiu, Y.; Liu, W.; Chen, W.; Chen, W.; Zhou, G.; Hsu, P. C.; Zhang, R.; Liang, Z.; Fan, S.; Zhang, Y.; Cui, Y. Efficient Solar-Driven Water Splitting by Nanocone $BiVO_4$-Perovskite Tandem Cells. *Sci. Adv.* **2016**, *2*, e1501764.
(37) Zhang, H.; Zhou, W.; Yang, Y.; Cheng, C. 3D $WO_3/BiVO_4$/Cobalt Phosphate Composites Inverse Opal Photoanode for Efficient Photoelectrochemical Water Splitting. *Small* **2017**, *13*, 1603840.
(38) Bhat, S. S. M.; Jang, H. W. Recent Advances in Bismuth Based Nanomaterials for Photoelectrochemical Water Splitting. *ChemSusChem* **2017**, *10*, 3001−3018.
(39) Bhachu, D. S.; Moniz, S. J. A.; Sathasivam, S.; Scanlon, D. O.; Walsh, A.; Bawaked, S. M.; Mokhtar, M.; Obaid, A. Y.; Parkin, I. P.;

https://dx.doi.org/10.1021/acs.inorgchem.0c01947
Inorg. Chem. 2020, 59, 13589−13597

Tang, J.; Carmalt, C. J. Bismuth Oxyhalides: Synthesis, Structure and Photoelectrochemical Activity. *Chem. Sci.* **2016**, *7*, 4832−4841.
(40) Liu, C.; Zhou, J.; Su, J.; Guo, L. Turning the Unwanted Surface Bismuth Enrichment to Favourable $BiVO_4$/BiOCl Heterojunction for Enhanced Photoelectrochemical Performance. *Appl. Catal., B* **2019**, *241*, 506−513.
(41) Fan, W.; Li, C.; Bai, H.; Zhao, Y.; Luo, B.; Li, Y.; Ge, Y.; Shi, W.; Li, H. An In-situ Photoelectroreduced Approach to Fabricate Bi/BiOCl Heterostructure Photocathode: Understanding the Role of Bi Metal for Solar Water Splitting. *J. Mater. Chem. A* **2017**, *5*, 4894−4903.
(42) Xing, Z.; Hu, J.; Ma, M.; Lin, H.; An, Y.; Liu, Z.; Zhang, Y.; Li, J.; Yang, S. From One to Two: *In-Situ* Construction of an Ultrathin 2D-2D Closelybonded Heterojunction from a Single-Phase Monolayer Nanosheet. *J. Am. Chem. Soc.* **2019**, *141*, 19715−19727.
(43) Sougrati, M. T.; Arayamparambil, J. J.; Liu, X.; Mann, M.; Slabon, A.; Stievano, L.; Dronskowski, R. Carbodiimides as Energy Materials: Which Directions for a Reasonable Future? *Dalton Trans.* **2018**, *47*, 10827−10832.
(44) Davi, M.; Mann, M.; Ma, Z.; Schrader, F.; Drichel, A.; Budnyk, S.; Rokicinska, A.; Kuśtrowski, P.; Dronskowski, R.; Slabon, A. An MnNCN-Derived Electrocatalyst for $CuWO_4$ Photoanodes. *Langmuir* **2018**, *34*, 3845−3852.
(45) Davi, M.; Drichel, A.; Mann, M.; Scholz, T.; Schrader, F.; Rokicinska, A.; Kuśtrowski, P.; Dronskowski, R.; Slabon, A. Enhanced Photoelectrochemical Water Oxidation Efficiency of $CuWO_4$ Photoanodes by Surface Modification with Ag_2NCN. *J. Phys. Chem. C* **2017**, *121*, 26265−26274.
(46) Zhao, W.; Liu, Y.; Liu, J.; Chen, P.; Chen, I.-W.; Huang, F.; Lin, J. Controllable Synthesis of Silver Cyanamide as a New Semiconductor Photocatalyst under Visible-Light Irradiation. *J. Mater. Chem. A* **2013**, *1*, 7942.
(47) Ressnig, D.; Shalom, M.; Patscheider, J.; Moré, R.; Evangelisti, F.; Antonietti, M.; Patzke, G. R. Photochemical and Electrocatalytic Water Oxidation Activity of Cobalt Carbodiimide. *J. Mater. Chem. A* **2015**, *3*, 5072−5082.
(48) Chen, Z.; Löber, M.; Rokicińska, A.; Ma, Z.; Chen, J.; Kuśtrowski, P.; Meyer, H. J.; Dronskowski, R.; Slabon, A. Increased Photocurrent of $CuWO_4$ Photoanodes by Modification with The Oxide Carbodiimide $Sn_2O(NCN)$. *Dalton Trans.* **2020**, *49*, 3450−3456.
(49) Corkett, A. J.; Chen, Z.; Bogdanovski, D.; Slabon, A.; Dronskowski, R. Band Gap Tuning in Bismuth Oxide Carbodiimide Bi_2O_2NCN. *Inorg. Chem.* **2019**, *58*, 6467−6473.
(50) Zhu, Y.; Liu, Y.; Lv, Y.; Ling, Q.; Liu, D.; Zhu, Y. Enhancement of Photocatalytic Activity for $BiPO_4$ *via* Phase Junction. *J. Mater. Chem. A* **2014**, *2*, 13041−13048.
(51) Zhang, X.; Liu, Y.; Zhang, G.; Wang, Y.; Zhang, H.; Huang, F. Thermal Decomposition of Bismuth Oxysulfide from Photoelectric Bi_2O_2S to Superconducting $Bi_4O_4S_3$. *ACS Appl. Mater. Interfaces* **2015**, *7*, 4442−4448.
(52) Hou, J.; Yang, C.; Wang, Z.; Zhou, W.; Jiao, S.; Zhu, H. In Situ Synthesis of $\alpha-\beta$ Phase Heterojunction on Bi_2O_3 Nanowires with Exceptional Visible-Light Photocatalytic Performance. *Appl. Catal., B* **2013**, *142−143*, 504−511.
(53) Morgan, W. E.; Stec, W. J.; Van Wazer, J. R. Inner-Orbital Binding-Energy Shifts of Antimony and Bismuth Compounds. *Inorg. Chem.* **1973**, *12*, 953−955.
(54) Ganguli, S.; Hazra, C.; Chatti, M.; Samanta, T.; Mahalingam, V. A Highly Efficient UV-Vis-NIR Active Ln^{3+}-Doped $BiPO_4$/$BiVO_4$ Nanocomposite for Photocatalysis Application. *Langmuir* **2016**, *32*, 247−253.
(55) Xu, H.; Xu, Y.; Li, H.; Xia, J.; Xiong, J.; Yin, S.; Huang, C.; Wan, H. Synthesis, Characterization and Photocatalytic Property of AgBr/$BiPO_4$ Heterojunction Photocatalyst. *Dalton. Trans.* **2012**, *41*, 3387−3394.
(56) Cong, Y.; Wang, J.; Jin, H.; Feng, X.; Wang, Q.; Ji, Y.; Zhang, Y. Enhanced Photoelectrocatalytic Activity of a Novel Bi_2O_3-$BiPO_4$ Composite Electrode for the Degradation of Refractory Pollutants under Visible Light Irradiation. *Ind. Eng. Chem. Res.* **2016**, *55*, 1221−1228.
(57) Lv, H.; Wu, X.; Liu, Y.; Zhang, P.; Cao, Y.; Ren, H. Photoreactivity and Mechanism of $BiPO_4$/WO_3 Heterojunction Photocatalysts under Simulant Sunlight Irradiation. *Ceram. Int.* **2018**, *44*, 6786−6790.
(58) Jiang, T.; Cheng, L.; Han, Y.; Feng, J.; Zhang, J. One-Pot Hydrothermal Synthesis of Bi_2O_3-WO_3 p-n Heterojunction Film for Photoelectrocatalytic Degradation of Norfloxacin. *Sep. Purif. Technol.* **2020**, *238*, 116428.
(59) Lv, Y.; Liu, Y.; Zhu, Y.; Zhu, Y. Surface Oxygen Vacancy Induced Photocatalytic Performance Enhancement of a $BiPO_4$ Nanorod. *J. Mater. Chem. A* **2014**, *2*, 1174−1182.
(60) Mao, Y.; Wang, P.; Li, L.; Chen, Z.; Wang, H.; Li, Y.; Zhan, S. Unravelling the Synergy between Oxygen Vacancies and Oxygen Substitution in BiO_{2-x} for Efficient Molecular-Oxygen Activation. *Angew. Chem., Int. Ed.* **2020**, *59*, 3685−3690.

https://dx.doi.org/10.1021/acs.inorgchem.0c01947
Inorg. Chem. 2020, 59, 13589−13597